Weather-Layer Dynamics of Baroclinic Eddies and Multiple Jets in an Idealized General Circulation Model

PAUL A. O'GORMAN AND TAPIO SCHNEIDER

California Institute of Technology, Pasadena, California

ABSTRACT

The general circulation and the behavior of multiple jets and baroclinic eddies are described for an atmosphere in which meridional potential temperature gradients and eddies are confined to a weather layer. The weather layer is separated from the frictional lower boundary by a statically stable barotropic layer with significant mass. Closure of the zonal momentum budget in the resulting circulation is achieved through ageostrophic meridional cells that extend to the lower boundary, at which momentum is dissipated. In a series of simulations with a multilevel primitive equation model, dynamic changes in the static stability of the weather layer are found to be critical in determining the scaling of the baroclinic eddies, an effect not captured in quasigeostrophic models. For simulations with a single jet in each hemisphere, the static stability of the weather layer adjusts so that a significant inverse energy cascade to scales larger than the Rossby deformation radius does not occur. The eddy length is found to scale with both the Rossby deformation radius and the Rhines scale. Simulations with larger planetary radii and low pole-to-equator temperature gradients exhibit multiple jets in each hemisphere. Eddy lengths and energies for the jet nearest the equator in each hemisphere have the same scaling as those in the single-jet simulations. Similar scalings are found for jets farther poleward but with different constants of proportionality that are consistent with more supercritical eddies. The local eddy length is found to have only a weak variation with latitude, and the local meridional jet spacing is found to scale with the local eddy length in all cases. Insights from the weather-layer simulations may be relevant to circulations in gas giant planets and the ocean.

1. Introduction

It is possible that on gas giant planets, baroclinic eddies occur in a weather layer above a barotropic deep layer (Williams 2003a,b; Ingersoll et al. 2004; Vasavada and Showman 2005). This is in contrast to the much studied case of Earth's troposphere, in which baroclinic eddies are active immediately above the planetary surface. Current theories may be inadequate to describe the equilibration of baroclinic eddies in a weather layer. Theories and simulations based on quasigeostrophic (QG) dynamics do not account for the feedback on static stability from the eddy heat fluxes, a feedback that can be expected to be important for eddy equilibration in primitive equation models (Gutowski 1985a,b; Zhou and Stone 1993). The theory of eddy equilibration of Schneider and Walker (2006) is based on the primitive equations and does allow for modification of the static stability by eddies, but the theory relies on eddy-induced intersections of isentropes with the planetary surface and is thus inapplicable to the dynamics of a weather layer. The eddy length is found to be important for the scaling of the interjet spacing in circulations with multiple zonal jets (Panetta 1993; Lee 2005), and so the equilibration of eddies may be expected to have implications for the jet spacing in a weather layer.

Here, in the absence of a theory of eddy equilibration for a weather layer, we set out the phenomenology in simulations with an idealized GCM. We document the scaling of eddy lengths and energies in the weather layer for a range of radiative forcings. Fundamental questions to be answered include whether there is a significant inverse energy cascade to length scales larger than the length scale of maximum linear baroclinic instability. The length scale of maximum linear baroclinic instability is given by the Rossby deformation radius, and an inverse energy cascade halted by the beta effect would have an eddy length given by the

Corresponding author address: Paul O'Gorman, California Institute of Technology, Mail Code 100-23, 1200 E. California Blvd., Pasadena, CA 91125.
E-mail: pog@caltech.edu

Rhines scale (Rhines 1975; Vallis and Maltrud 1993). We compare the scaling of the eddy length in the weather layer to estimates of the Rossby deformation radius and the Rhines scale. In the case of circulations with multiple jets in each hemisphere, we examine the meridional interjet spacing, as well as differences in the scalings of eddy lengths and energies for the different jets. We also examine the general circulation and zonal momentum balance of the weather layer and the barotropic layer beneath.

In addition to understanding the dynamics of the weather layer for its own sake, a second goal of our study is to further the understanding of the simulations and theory of Schneider and Walker (2006), in which baroclinic eddies are active directly above a lower boundary with a significant temperature gradient (as on earth). Schneider and Walker (2006) found that no significant inverse energy cascade occurred to scales larger than that of the linearly most unstable baroclinic wave, corresponding to a state in which nonlinear eddy–eddy interactions are not important in setting the eddy length. The simulations of Schneider and Walker (2006) differ from QG two-layer model dynamics (which do allow an important role for eddy–eddy interactions in setting the eddy length) both because the static stability is dynamically determined and because of eddy-induced intersections of isentropes with the lower boundary (Schneider 2005). It is therefore interesting to evaluate if the eddy equilibration is different in a weather layer in which there are no eddy-induced intersections of isentropes with the lower boundary but in which the static stability is dynamically determined.

To simulate a weather layer, we have constructed an idealized primitive equation GCM in which baroclinic eddies are confined away from the lower boundary. Radiative forcing is represented as Newtonian relaxation to a radiative equilibrium state with meridional temperature gradients only in a weather layer overlying a statically stable barotropic layer. We have performed a series of simulations with the idealized GCM, varying parameters such as the planetary radius and the meridional temperature gradient in radiative equilibrium. We have obtained a wide variety of circulations with both single and multiple jets in each hemisphere.

In our simulations of a weather layer, we do not attempt to replicate the parameter regime of the gas giant planets, or features such as their mean pole-to-equator temperature difference, but rather focus on the dynamics of the eddy equilibration in a weather layer in which the static stability can respond to eddy fluxes. The dynamics of eddies in weather layers on gas giant planets are more complicated than those considered here because there the eddies can derive energy from both

differential solar heating and from convective heat fluxes from the planetary interior (Busse 1994; Ingersoll et al. 2000). In addition, we have a statically stable barotropic layer rather than the statically neutral convective interior expected on the gas giant planets (Vasavada and Showman 2005). Our study of the equilibration of baroclinic eddies in a weather layer is complementary to the weather-layer studies of Williams (2003a,b), who investigated, among other things, the effects on the circulation of different static stability profiles and different depths of the barotropic layer.

Section 2 describes the idealized GCM, and section 3 describes the general circulation in a typical simulation. Sections 4 and 5 discuss the scaling of the baroclinic eddies, and section 6 discusses the meridional interjet spacing in a series of simulations. Section 7 summarizes the conclusions, and section 8 discusses further work and the possible relevance of the simulations to gas giant planets and the ocean.

2. Idealized GCM with weather layer

We use a dry idealized GCM based on the Geophysical Fluid Dynamics Laboratory (GFDL) dynamical core, similar to that used by Held and Suarez (1994), with standard earth parameters except where noted. The lower boundary of the GCM is zonally symmetric, uniform with no topography, and thermally insulating. Subgrid-scale dissipation is represented by ∇^8 hyperdiffusion in the vorticity, divergence, and temperature equations. The same vertical resolution is used in all simulations, with 30 unevenly spaced sigma (σ) levels. The wind is damped near the lower boundary by Rayleigh drag with a damping coefficient decreasing linearly in σ from 1 day^{-1} at the lower boundary to zero at $\sigma = 0.85$.

Radiative forcing is represented as Newtonian relaxation of temperatures to a radiative equilibrium with three horizontal layers joined using a smoothing function; see Fig. 1 for an example. The uppermost radiative-equilibrium layer ($0 < \sigma < 0.2$) is a statically stable "stratosphere" with approximately constant temperature. The lowermost layer ($0.6 < \sigma < 1$) is also statically stable. The middle layer is the weather layer ($0.2 < \sigma < 0.6$), in which the radiative-equilibrium temperature distribution is modeled after that of Held and Suarez (1994). The weather-layer potential temperature θ_w in radiative equilibrium is given by

$$\theta_w = \theta_p + (\Delta_h - \Delta_z \log\sigma) \cos^2\phi, \qquad (1)$$

where ϕ is latitude and $\theta_p = 260$ K is the temperature at the poles. The parameter Δ_z controls the static stability, and Δ_h controls the meridional temperature gra-
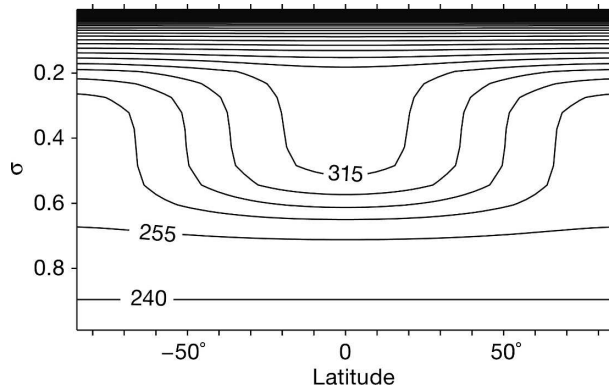
FIG. 1. Radiative-equilibrium potential temperature (K). The contour interval (CI) is 15 K. Figs. 1–9 are for the simulation with $\Delta_h = 60$ K, $\Delta_z = 2$ K, and twice Earth's radius (though the radiative equilibrium shown here does not depend on the planet radius).
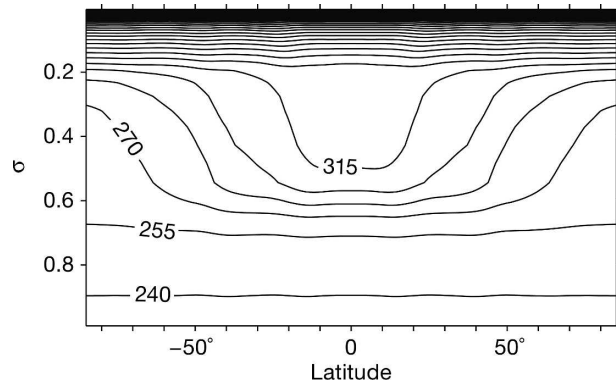

FIG. 2. Potential temperature (K). The CI is 15 K. Fields shown in Figs. 2–8 are based on zonal and time averages. For all statistics presented, an average between the statistically identical Northern and Southern Hemispheres has been taken.

dient. The radiative relaxation time is 1 day in the lowermost layer and 40 days elsewhere. A complete description of the radiative-equilibrium temperature distribution and relaxation time distribution is given in the appendix. The radiative equilibrium is statically stable everywhere (approaching neutrality at the poles in the weather layer), so that a convection scheme is not needed. The static stability of the lowermost layer is greater than that of the weather layer; this was found to be necessary to confine eddy fluctuations to the weather layer and prevent them from interacting with the lower boundary. (A sufficiently strong increase of density across a neutrally stratified lowermost layer presumably would also prevent eddies from interacting significantly with the lower boundary, but this would require a lowermost layer extending over several density scale heights.)

A series of simulations was performed with different Δ_h and Δ_z to examine the behavior of the eddy lengths, energies, and jet spacings and to see if there exists a regime in which eddy–eddy interactions play an important role in setting the eddy length. The basic series of 40 simulations is at T42 horizontal resolution with $\Delta_h = 30, 60, \ldots, 270$ K and $\Delta_z = 2, 5, 10, 20$ K. To allow for multiple jets, we also include simulations with a planet radius two and four times that of Earth, with horizontal resolutions of T85 and T127, respectively, and $\Delta_z = 2$ K. Simulations with twice Earth's radius have Δ_h values ranging from 60 to 240 K. Simulations with four times earth's radius have Δ_h values ranging from 90 to 240 K. Results are averaged over 200 days after a statistically steady state was reached for each simulation. Pole-to-equator temperature differences in dynamical equilibrium are found to scale linearly with those in radiative equilibrium, with a reduction in value from radiative to

dynamical equilibrium of approximately 25%. However, eddies render the weather layer significantly more statically stable in dynamical equilibrium than it is in radiative equilibrium (cf. Figs. 1, 2, and 3).

3. The general circulation of the weather layer

We discuss a typical simulation (Figs. 1–9) with twice earth's radius and radiative forcing parameters $\Delta_h = 60$ K and $\Delta_z = 2$ K. The radiative-equilibrium temperature distribution (Fig. 1) causes meridional potential temperature gradients and baroclinic eddies to be confined to the weather layer above a largely barotropic lowermost layer (see Figs. 2 and 4). The meridional gradient of potential vorticity (PV) along isentropes is reversed in part of the lower half of the weather layer, allowing for baroclinic instability. The reversal of the PV gradient is achieved through the meridional gradient in isen-
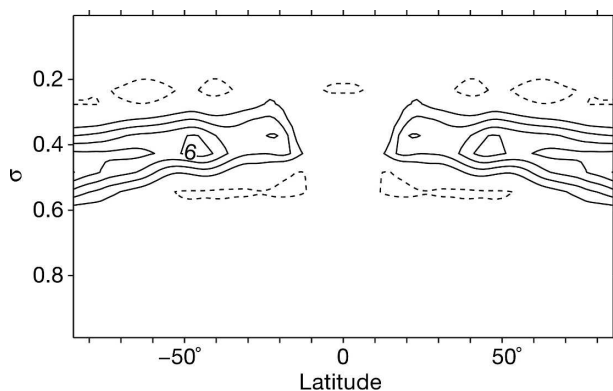

FIG. 3. Change in buoyancy frequency (10^{-3} s^{-1}) between radiative and dynamical equilibrium. Dashed contours indicate negative values. The zero contour has been omitted. The CI is 1.5×10^{-3} s^{-1}.
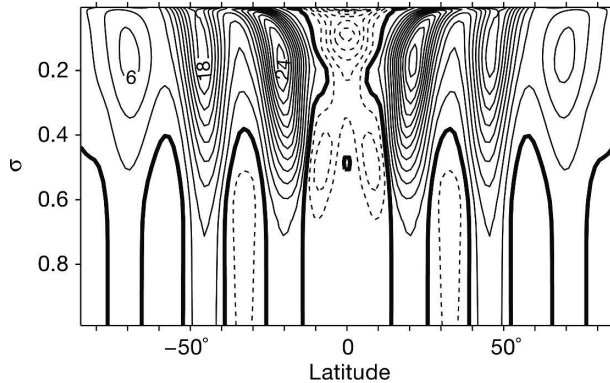
FIG. 4. Zonal wind (m s^{-1}). The zero contour is marked with a thicker line, and dashed contours indicate negative values. The CI is 2 m s^{-1}.

FIG. 6. Isentropic mass flux streamfunction (10^9 kg s^{-1}). The zero contour is omitted, and dashed contours indicate negative values. The CI is 10^{10} kg s^{-1}.

tropic density, $\rho_\theta = -g^{-1}\partial_\theta p$, as can be inferred from the contours of mean potential temperature in Fig. 2. The vertical spacing of potential temperature contours and thus the isentropic density increase poleward along isentropes in the lower half of the weather layer, whereas the isentropic density generally decreases poleward along isentropes in the upper half of the weather layer. The QG two-layer model thus more closely resembles the weather layer than Earth's atmosphere, in which the reversal of the PV gradient occurs in the layer of isentropes that intersect the surface (Schneider 2005). However, unlike in the QG two-layer model, eddy heat fluxes affect the static stability, with an increase in static stability compared with radiative equilibrium in the middle levels of the weather layer and a decrease above and below these levels (Fig. 3).

The transition from the weather layer to the barotropic layer is not apparent in the Eulerian mass streamfunction, shown in Fig. 5, but is apparent in the mass
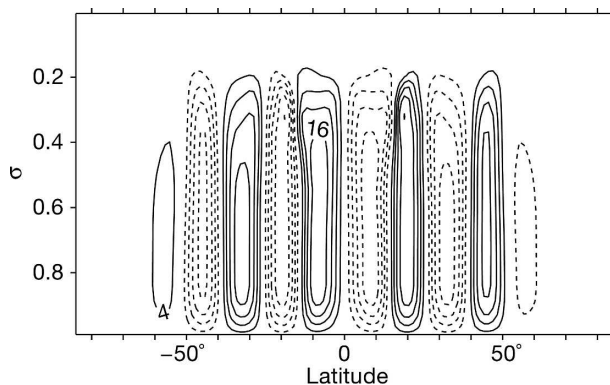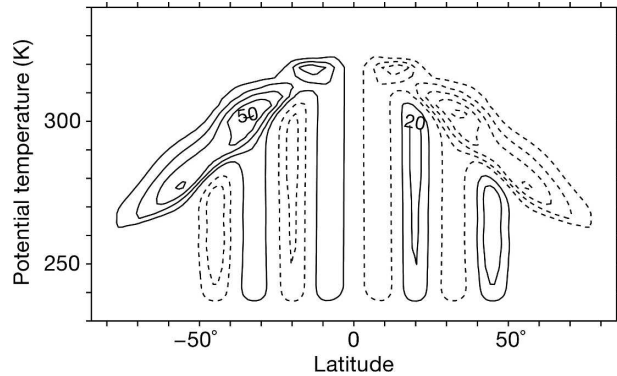

FIG. 5. Eulerian mass flux streamfunction (10^9 kg s^{-1}). The zero contour is omitted, and dashed contours indicate negative values. The CI is 4×10^9 kg s^{-1}.

streamfunction in isentropic coordinates, shown in Fig. 6. The isentropic streamfunction consists primarily of one overturning cell in each hemisphere in the weather layer and a series of ageostrophic cells in the lowermost layer. Because there are no eddies near the lower boundary, the isentropic mass flux streamfunction is similar to the QG transformed Eulerian mean circulation (not shown here) everywhere, unlike in Earth's atmosphere where they differ near the surface (Held and Schneider 1999).

The Coriolis force on the meridional geostrophic mass flux in an isentropic layer balances the form or pressure drag on the layer (Andrews 1983), so that the vertical integral of the meridional geostrophic mass flux vanishes in the absence of surface pressure drag due to topography at the lower boundary (Schneider 2007). In our simulations, therefore, the geostrophic and ageostrophic circulations close individually, and we can define geostrophic and ageostrophic mass streamfunctions individually by vertical integration of the geostrophic or ageostrophic meridional mass fluxes. The resulting streamfunctions in Fig. 7 show that the meridional mass flux in the extratropics is largely associated with the geostrophic velocity in the weather layer and with the ageostrophic velocity in the lowermost layer. In section 4, we use the geostrophic mass streamfunction to define the dynamical weather-layer depth.

Multiple jets in each hemisphere occur for many simulations, predominantly those with smaller pole-to-equator temperature gradients and with planetary radius greater than Earth's. The multiple jets are evident in the zonal wind (Fig. 4) and in the vertically integrated eddy momentum flux convergence (Fig. 8, right axis). We will use the term "jet" to refer to local maxima in the westerlies in the weather layer. These zonal wind maxima are associated with westerlies at the lower boundary and with a region of enhanced barocli-
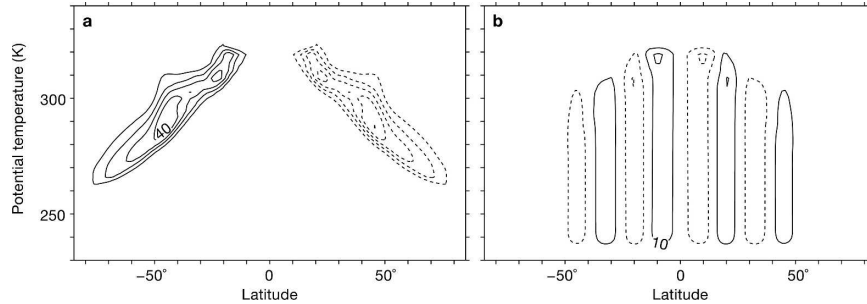
FIG. 7. Isentropic mass flux streamfunctions (10^9 kg s^{-1}) related to (a) geostrophic and (b) ageostrophic meridional mass flux. The zero contour is omitted, and dashed contours indicate negative values. The CI is 10^{10} kg s^{-1}.

nicity (Panetta 1993) and eddy momentum flux convergence. The eddy momentum flux convergence occurs because the baroclinic eddies in the weather layer converge zonal momentum into regions where they are generated (cf. Held 1975, 2000; Simmons and Hoskins 1978; Ioannou and Lindzen 1986). Zonal momentum balance is achieved by the ageostrophic meridional cells, which extend to near the lower boundary, where the Rayleigh drag acting on the zonal wind balances the Coriolis force on the meridional flow (Ekman balance). The vertically integrated eddy momentum flux convergence shown in Fig. 8 (right axis) is equal to the stress exerted by the atmosphere on the lower boundary and is approximately proportional to the mean zonal wind at the lower boundary. The ageostrophic cells may also be viewed as the response required by the principle of "downward control" to the eddy fluxes in the weather

layer (Haynes et al. 1991). The streamfunctions of the ageostrophic cells in the lowermost layer are of alternating signs, consistent with Ekman balance at the lower boundary and the alternating signs of the zonal wind at the lower boundary, and the eddy momentum flux convergence and divergence in the weather layer.

4. Eddy scaling for single-jet simulations

In all simulations, the global energy spectra show an approximate n^{-3} power-law range in spherical wavenumber n with no indication of an inverse energy cascade to scales larger than the scale of baroclinic instability (Fig. 9). For simulations with a single jet in each hemisphere, this is consistent with eddy energy residing at the baroclinically most unstable wavenumber. Thus, for single-jet simulations we expect the eddy length to scale with the Rossby deformation radius, and we expect approximate equipartition between eddy available potential energy and baroclinic eddy kinetic energy (Held and Larichev 1996). For simulations with multiple jets in each hemisphere, the eddy lengths for each jet must be examined individually.
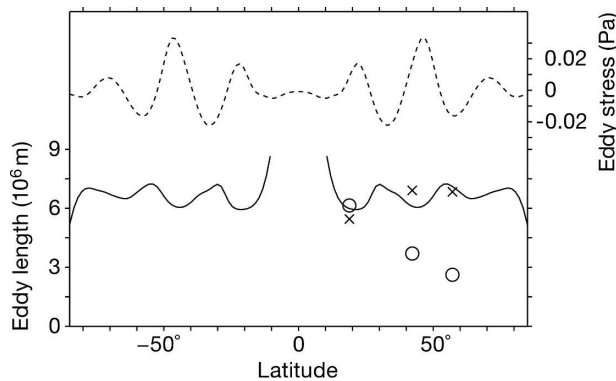

FIG. 8. Eddy length (solid line and left vertical axis) and vertically integrated eddy momentum flux convergence (eastward stress) (dashed line and right vertical axis) vs latitude. Eddy lengths at latitudes within $10°$ of the equator are not shown. Rhines scale (crosses) and Rossby first deformation radius (circles) are shown at the three meridional eddy potential temperature flux maxima used as reference latitudes. For ease of comparison, the Rhines scale has been divided by a constant factor 0.62 corresponding to the slope in Fig. 11.
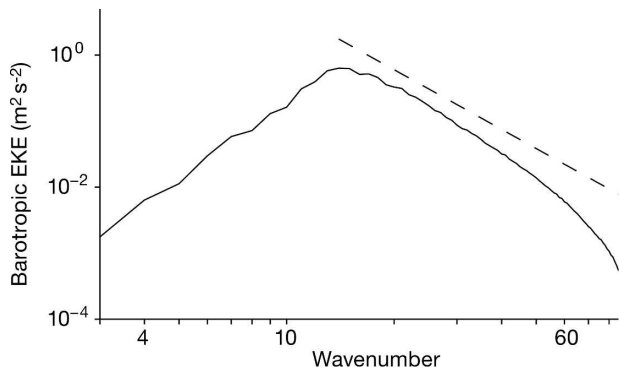

FIG. 9. Barotropic eddy kinetic energy spectrum as a function of spherical wavenumber n. The dashed line indicates an n^{-3} power law.

We first discuss the simulations with a single jet in each hemisphere. We examine the eddy lengths, energies, and a measure of the supercriticality to baroclinic instability (Figs. 10–13). To evaluate the Rossby deformation radius, Rhines scale, and eddy energies, we need to define a reference latitude and appropriate averages. The Coriolis parameter f and its meridional gradient β are evaluated at the reference latitude, which is chosen to be the latitude ϕ_m of maximum eddy potential temperature flux $\overline{v'\theta'}\cos\phi$ at $\sigma = 0.5$, where v' and θ' are the eddy velocity and potential temperature. The overbar indicates a zonal and time average, as well as an average between the statistically identical Northern and Southern Hemispheres.

Simulations with one eddy potential temperature flux maximum in each hemisphere are considered to be single-jet simulations, and, in general, the number of jets is counted using the number of such maxima, excluding maxima within 4° latitude of the equator. Some of the simulations have a subtropical jet in the weather layer that is not associated with significant eddy momentum flux convergence or horizontal eddy temperature flux. Use of the eddy potential temperature flux to identify jets, rather than the zonal wind in the weather layer, avoids counting these subtropical jets, which we exclude from our analysis.

a. Eddy length scale

To characterize the eddy length scale, we use the energy-containing zonal wavenumber m_e, calculated from the zonal spectrum E_m of the vertically averaged meridional velocity using the integral definition

$$m_e^2 = \frac{\Sigma_m E_m}{\Sigma_m m^{-2} E_m}, \tag{2}$$

where the zonally symmetric wavenumber zero is excluded. Our choice of the exponent of m in the integral definition gives an energy-containing zonal wavenumber that is empirically found to be close to the wavenumber of the maximum of the zonal energy spectrum. Length scales L and zonal wavenumbers m at a given latitude ϕ are related by $m = 2\pi a \cos\phi/L$.

The eddy length scale outside the tropics is shown for one simulation in Fig. 8 (left axis). The eddy length scale does not vary strongly with latitude, except in the tropics where the integral definition (2) of energy-containing wavenumber does not work well. Note that in Fig. 8 the latitudes ϕ_m, where the Rossby deformation radius and Rhines scale are evaluated, are displaced equatorward from the corresponding maxima in eddy momentum flux convergence. This is especially true of the third jet from the equator, which is an atypi-

cal example. We nonetheless use the eddy potential temperature flux rather than, say, the eddy momentum flux convergence to identify reference latitudes for the jets because using the potential temperature flux gives cleaner scaling results, especially for the single-jet simulations.

For the comparisons below between Rossby deformation radius, Rhines scale, and eddy length, we evaluate the energy-containing wavenumber at the reference latitude ϕ_m and convert from length scales to zonal wavenumbers also using the reference latitude ϕ_m. We use zonal rather than spherical wavenumbers for ease of comparison with the simulations with multiple jets in each hemisphere discussed in section 5, where eddy lengths for different jets are needed.

b. Rossby deformation radius

We use the first Rossby deformation radius as an estimate of the length scale of maximum linear baroclinic instability. The Rossby deformation radius is calculated as $L_D = 2\pi \langle N_p \Delta_p \rangle/f$, a scaling estimate of the first baroclinic Rossby deformation radius, where Δ_p is the pressure difference over the weather layer. The angle brackets denote an average taken horizontally over a 6° latitude band about the reference latitude ϕ_m and vertically over the middle of the weather layer from $\sigma = 0.35$ to $\sigma = 0.45$, following zonal and time averages. The static stability parameter N_p is defined by $N_p^2 = -(\overline{\rho\theta})^{-1}\partial_p\overline{\theta}$ where ρ is the density and θ is the potential temperature (cf. Schneider and Walker 2006). We use the geostrophic isentropic mass streamfunction (Fig. 7a) to identify the top and bottom of the weather layer, and thus via interpolation the pressure difference Δ_p. The top and bottom of the weather layer at a given latitude are identified as the levels at which the geostrophic isentropic mass streamfunction is $1/e$ times its maximum value at that latitude.

The eddy length (energy-containing scale) scales with the Rossby deformation radius (Fig. 10). As the meridional temperature gradient is increased through changes in the radiative parameter Δ_h, the static stability is increased by the eddies, and the eddy length and Rossby deformation radius increase. Since the dynamical-equilibrium static stability is often much greater than that given by the radiative equilibrium, the eddy length is relatively insensitive to the radiative-equilibrium static stability controlled by Δ_z.

c. Rhines scale

The beta effect inhibits nonlinear upscale transfer of eddy energy, and a measure of the length scale at which the beta effect becomes important is given by the
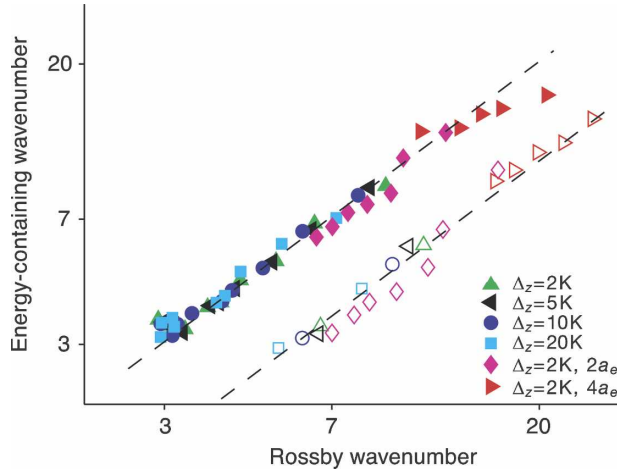
FIG. 10. Energy-containing vs Rossby zonal wavenumber. In Figs. 10–14, different plotting symbols denote sets of simulations with different planet radii or values of the static stability at radiative equilibrium, Δ_z. Simulations with two and four times Earth's radius are labeled $2a_e$ and $4a_e$. For each plotting symbol, there are several simulations with different meridional temperature gradients at radiative equilibrium, Δ_h. Filled symbols indicate the jet nearest the equator (the only jet for simulations with a single jet in each hemisphere). Open symbols indicate the next jet poleward. The dashed lines indicate linear relationships with zero intercepts and slopes 1.0 and 0.52, corresponding to the first and second jets poleward, respectively. The slopes of the dashed lines were determined by least-squares fits of slope-1 lines to the logarithms of the wavenumbers.
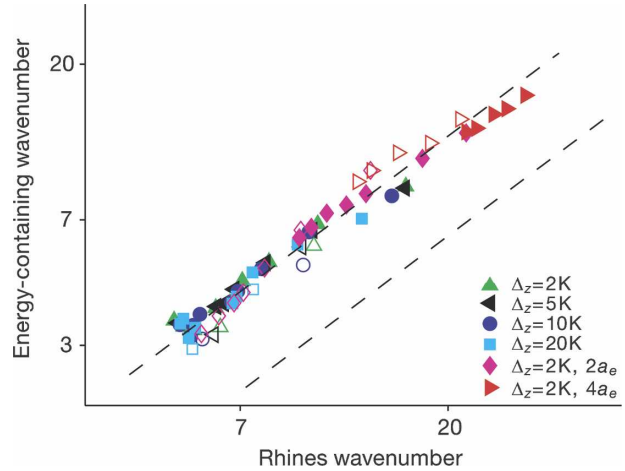

FIG. 11. Energy-containing vs Rhines zonal wavenumber. Symbols are as described in Fig. 10. The upper dashed line is a linear fit using the same method as in Fig. 10, but using data points from both jets, and has slope 0.62. The lower dashed line is shown for reference and is chosen so that the ratio of the slopes of the upper and lower dashed lines is the same as in Fig. 10.

Rhines scale (Rhines 1975; Vallis and Maltrud 1993). We define the Rhines scale as $L_\beta = 2\pi \, \mathrm{EKE}^{1/4}/\beta^{1/2}$, where EKE is the average of the barotropic eddy kinetic energy per unit mass over a 6° latitude band about the reference latitude ϕ_m. The Rhines scale so defined is a scaling estimate and can only be expected to be significant to within a constant factor of order one.

We find that the eddy length also scales with the Rhines scale (Fig. 11). In the simulations of Schneider and Walker (2006), the eddy length was found to be larger than the Rhines scale in a circulation regime in which convection sets the static stability. There is no convection scheme in the simulations presented here, and the effect of the positive radiative-equilibrium static stability is too weak to play the same role.

d. Supercriticality

The concept of a supercriticality that measures the baroclinic instability of a flow has been useful for understanding both two-layer (Held and Larichev 1996) and continuously stratified (Pedlosky 1979) QG models. Schneider and Walker (2006) found that a similar supercriticality based on near-surface potential temperature gradients was appropriate in characterizing

the turbulence in simulated atmospheres with nonzero surface potential temperature gradients. We have already discussed in section 3 how the reversal of the mean PV gradient in the lower half of the weather layer is similar to the reversal of the PV gradient in the lower layer of a baroclinically unstable QG two-layer model. This suggests that it may be appropriate to consider a supercriticality analogous to that of the two-layer QG model as a measure of the baroclinic instability of the weather layer. We define the supercriticality of the weather layer as

$$S_c = -\frac{f\partial_y\theta}{\beta\Delta_v}, \qquad (3)$$

where the vertical potential temperature difference is $\Delta_v = -\partial_p\theta \, \Delta_p/2$. The definition (3) should be understood as a heuristic instability measure given the inexact analogy with the QG two-layer model. The mean scaled temperature gradient $-f\langle\partial_y\theta\rangle/\beta$ is plotted against the mean vertical potential temperature difference $\langle\Delta_v\rangle$ in Fig. 12, which suggests that the supercriticality evaluated in the middle of the weather layer remains of order one. The static stability, as measured by Δ_v, increases with the meridional potential temperature gradient, resulting in a constant supercriticality. Changes in the latitude at which the Coriolis parameter and its gradient are evaluated are also important; neglecting this variation in latitude would lead to considerable scatter in Fig. 12, especially between simulations with different planetary radii. This suggests that it is the supercritical-
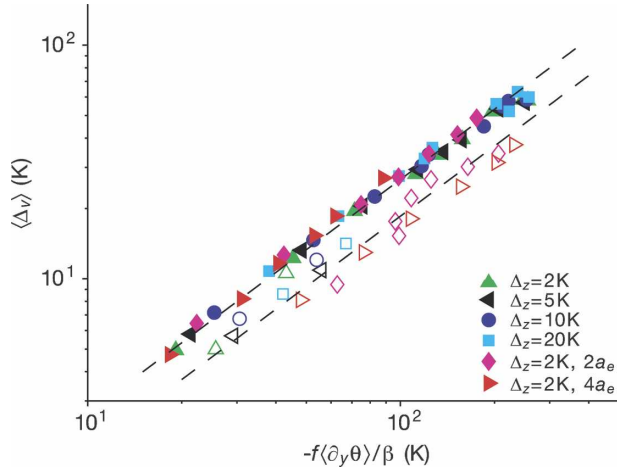
FIG. 12. Vertical potential temperature difference $\langle \Delta_v \rangle$ vs scaled meridional temperature gradient $-f \langle \partial_y \theta \rangle / \beta$. Dashed lines represent constant supercriticalities of 3.8 and 5.4. Symbols and line-fitting method are as described in Fig. 10.

FIG. 13. Baroclinic eddy kinetic energy vs eddy available potential energy. Dashed lines are EKE = 0.94 EAPE and EKE = 0.48 EAPE. Symbols and line-fitting method are as described in Fig. 10.

ity rather than the isentropic slope that is dynamically significant.

e. Eddy energies

The eddy available potential energy scales with the baroclinic eddy kinetic energy (Fig. 13). The eddy available potential energy was calculated using the quadratic approximation of Lorenz (1955) transformed to σ coordinates, and the energies per unit mass have been averaged over a 6° latitude band about the reference latitude ϕ_m. The equipartition of eddy energies is consistent with there being no significant inverse energy cascade beyond the scale of the linearly most unstable wave in the single-jet simulations (Held and Larichev 1996).

5. Eddy scaling for multiple-jet simulations

For simulations with multiple jets in each hemisphere, we consider the scalings of eddies for each jet separately. Eddy lengths, energies, and the supercriticality were evaluated using the definitions described in section 4 but on a jet-by-jet basis.

The scaling of eddy lengths and energies and of the supercriticality are the same for the jet nearest the equator as for the single-jet simulations (Figs. 10–13). For the next jet poleward, the eddy length also scales with the Rhines scale in the same way, but the eddy energies, Rossby deformation radius, and supercriticality scalings are different. The eddy available potential energy and baroclinic eddy kinetic energy are proportional to one another, but with a different constant of proportionality. Similarly, the eddy length and Rossby deformation radius are proportional but with a differ-
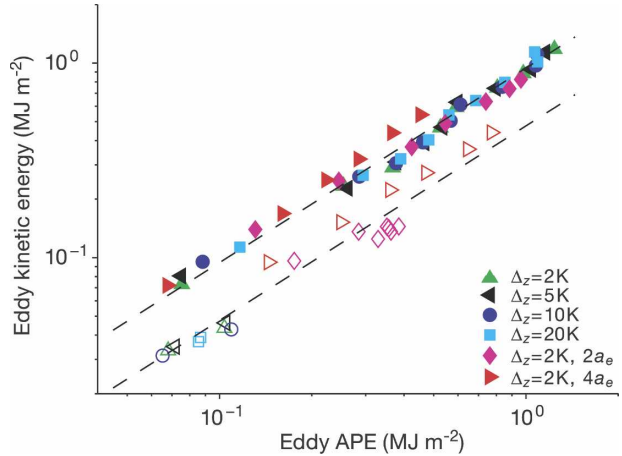
ent constant of proportionality. The supercriticality is again approximately constant for different radiative-equilibrium temperature gradients, but it is greater than for the first jet.

Results (not shown) for the third jet from the equator show a continued trend. For example, the ratio of eddy length to Rossby deformation radius is greater than for the second jet from the equator. We restrict our analysis to the first two jets nearest the equator in each hemisphere for clarity of presentation and because there are too few simulations with a well-defined third jet to make the scalings clear.

The ratio of eddy available potential energy to baroclinic eddy kinetic energy, the ratio of eddy length to Rossby deformation radius, and the supercriticality are all greater for the second jet than for the first jet, whereas the scaling of eddy length to Rhines scale remains the same, suggesting that there may be an inverse energy cascade beyond the scale of the linearly most unstable wave for the second jet. Unfortunately, the zonal energy spectra based on the meridional velocity are noisy and do not confirm or contradict this hypothesis definitively, especially given that only a short inverse energy cascade without a proper inertial range could be expected. The global energy spectra (Fig. 9) have significant contributions from the eddy kinetic energy of all the jets, including the jet nearest the equator, and so are not definitive for the behavior of jets farther poleward.

6. Jet separation scaling

We present a jet-by-jet analysis of the meridional jet spacing for simulations with two or more jets in each
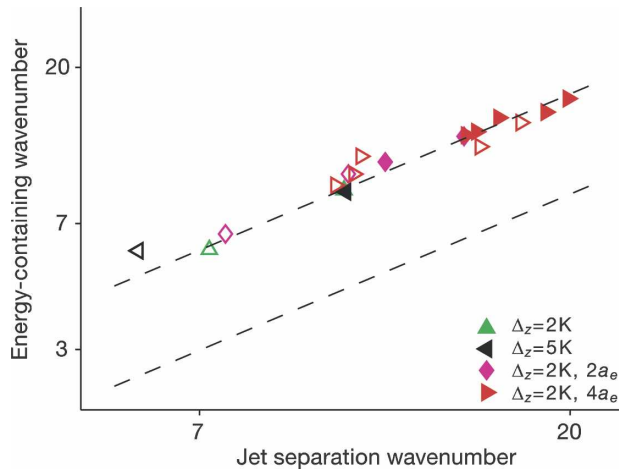
FIG. 14. Energy-containing vs jet separation zonal wavenumber. Symbols are as described in Fig. 10, but only simulations with two well-defined jet widths in each hemisphere are shown. The upper dashed line is a linear fit using the same method as in Fig. 10, but using data points from both jets, and has slope 0.84. The lower dashed line is shown for reference and is chosen so that the ratio of the slopes of the upper and lower dashed lines is the same as in Fig. 10.

hemisphere, where the number of jets is counted using the eddy potential temperature flux maxima as in section 4. We do this by associating with each jet a meridional width defined as the distance between zonal wind minima on either side of the zonal wind maximum of the jet. Zonal wind minima and maxima are determined using the zonal wind at the lower boundary to avoid considering subtropical jets that are not associated with significant eddy activity. Several simulations with two or more eddy potential temperature flux maxima do not have well defined jet widths by this definition and are excluded from our jet separation analysis, as are zonal wind maxima within 4° latitude of the equator.

The energy-containing zonal wavenumber for each jet is found to scale with the jet-spacing wavenumber (Fig. 14) with a constant of proportionality of 0.84. Thus, the meridional jet spacing is approximately given by the eddy length, and this also holds for the third jet from the equator when it exists (not shown). In our simulations, the eddy length is typically constant over a wide range of extratropical latitudes (cf. Fig. 8), and thus we expect the meridional jet spacing to be relatively constant over this range. This may be compared with the jet spacing on Jupiter, which also does not show a strong trend in latitude outside the tropics (Porco et al. 2003; Smith 2004).

It may seem surprising that the jet spacing is of the order of the Rossby deformation radius for the jet nearest the equator where eddy–eddy interactions are not important in determining the eddy length, given that the baroclinically most unstable wave has very large meridional scale. It is possible, however, that even weak eddy–eddy interactions can isotropize the eddies, and Pedlosky (1975) showed that there is a secondary baroclinic instability of the most unstable wave on the meridional scale of the Rossby deformation radius.

7. Conclusions

We have examined the general circulation and the scalings of eddy lengths and energies in weather-layer simulations with both single and multiple jets in each hemisphere. The zonal-mean circulation of the weather layer in isentropic coordinates clearly distinguishes between the circulations in the weather layer and lower barotropic layer. The isentropic mass flux streamfunction can be decomposed into geostrophic and ageostrophic parts (Fig. 7), with the geostrophic part (eddy mass transport) being confined to the weather layer, and the ageostrophic part extending to the region of momentum dissipation near the lower boundary to close the zonal momentum budget.

For the jet nearest the equator, we have shown how changes in the thermal structure of the weather layer involving changes in the static stability allow the supercriticality to remain of order one. The eddy length was found to scale with the first Rossby deformation radius and the Rhines scale. For simulations with multiple jets in each hemisphere, the supercriticality of the second jet remains approximately constant for different radiative forcings, but with a higher value than for the first jet. Similar changes in constants of proportionality occurred for eddy energy and Rossby deformation radius scalings. The eddy length continues to scale with the Rhines scale with the same constant of proportionality as for the first jet. As in the case of the jet nearest the equator, the static stability in the region of the second jet is significantly increased in dynamical equilibrium relative to radiative equilibrium (cf. Fig. 3). But the latitude dependencies of the f/β factor in the supercriticality and the radiative-equilibrium temperature distribution mean that greater changes in static stability or meridional temperature gradient are needed to achieve a given supercriticality for the second jet compared with the jet nearest the equator.

We have also examined the meridional jet spacing in circulations with multiple jets in each hemisphere. The local meridional jet spacing was found to scale with the eddy length, and thus with the local Rhines scale. The jet spacing and eddy length do not show a strong variation with latitude in our simulations (cf. Fig. 8), but this may not be the case for weather layers with a greater number of jets than in our simulations.

The eddy equilibration of the weather layer can be compared with eddy equilibration in simpler models and with the baroclinic adjustment hypothesis (Stone 1978). In agreement with the simulations of Stone and Branscome (1992) with a QG two-layer model, there is a tendency for the isentropic slope in dynamical equilibrium to be reduced compared with that in radiative equilibrium, and the QG two-layer supercriticality is close to constant, although greater than one. The behavior of the weather layer is closer to the two-level model simulations of Zhou and Stone (1993) with dynamically determined static stability. Nevertheless, the dynamical equilibrium of the circulations is not neutral with respect to baroclinic instability, as would be predicted by the baroclinic adjustment hypothesis of Stone (1978), and there are significant positive and negative PV gradients at dynamical equilibrium.

A second goal of this study was to compare with the simulations and theory of Schneider and Walker (2006). The eddy equilibration is not sufficiently qualitatively different in the weather layer (at least for the jet nearest the equator) to demonstrate that eddy-induced surface intersections of isentropes are important for eddy equilibration, although the effects of a dynamically determined static stability are clearly important both here (cf. Fig. 12) and in Schneider and Walker (2006).

8. Discussion and relevance to gas giant planets and the ocean

The question remains whether there is a tendency in the weather layer for eddy–eddy interactions to play a more important role in setting the eddy length for jets farther poleward. It may be the case that a consistent local analysis for different jets of the sort attempted here is not appropriate. For example, the link between the length scales of the linearly most unstable modes calculated globally for the weather layer and the simple Rossby deformation radius used here is unclear a priori. Approximations such as that of Wentzel–Kramers–Brillouin–Jeffreys (WKBJ), which rely on scale separation, may not be applicable because the mean fields vary on the meridional jet scale, which is comparable to the most unstable wavelength.

Several ways to resolve the issue include studying larger or more rapidly rotating planets with more jets or performing a linear stability analysis for the simulations with multiple jets to determine the linearly most unstable wavenumbers directly. Simulations with a primitive equation model in a channel on a beta plane may also be instructive.

a. Relevance to gas giant planets

To the extent that baroclinic eddies in a weather layer play a role in the large-scale turbulence of gas giant planets, the above results regarding the supercriticality, eddy length and energy scalings, and the interjet separation would be applicable. The more realistic case of a deep barotropic layer that is statically neutral and convecting remains as a subject for further study. The relatively small depth of our barotropic layer may not be a severe limitation insofar as increasing the depth of the barotropic layer may not alter the circulation qualitatively other than to increase the vertical scale of the ageostrophic circulation cells, as was found to be the case in the weather-layer simulations of Williams (2003a). Of course, our results are only appropriate for the shallow part of the atmosphere where the traditional approximation (the thin-shell approximation with a consistent simplification of the Coriolis force) is valid.

To more closely link our simulations with the circulations of gas giant planets, the zonal momentum balance must be more closely examined. In our simulations, the eddy momentum flux convergence in the weather layer is balanced by Rayleigh drag on the zonal wind near the lower boundary. It is unclear what the corresponding dissipation mechanism would be on a gas giant planet. Such a dissipation mechanism is necessary in the case of baroclinic eddies in the weather layer, since if we remove the Rayleigh drag in our simulations, eddy activity vanishes, a phenomenon known as the barotropic governor (James and Gray 1986).

b. Relevance to the ocean

An analogy can be drawn between the baroclinic eddies in the weather layer and mesoscale eddies in the thermocline of the ocean. The lowermost layer of the weather-layer simulation then corresponds to the abyss, with Rayleigh friction near the lower boundary corresponding to bottom drag. The eddies cannot be completely confined to the thermocline since the abyss is nearly adiabatic, so that in the heat budget of the abyss the ageostrophic circulation must be balanced by eddy fluxes. However, the idea of a deep meridional cell extending to the region of significant bottom drag as a means to close the zonal momentum budget is still applicable. The scaling of the eddy lengths and energies for different jets and the importance of the adjustment of the static stability should also be relevant to eddies in the ocean.

APPENDIX

Radiative-Equilibrium Temperature and Damping Time Distributions

The radiative-equilibrium potential temperature θ is given by the combination of uppermost, weather, and lowermost layers,

$$\theta = \theta_u s_u + \theta_w s_l (1 - s_u) + \theta_l (1 - s_l). \quad \text{(A1)}$$

The smoothing functions are defined by $s_l = s(\sigma, \sigma_l)$ and $s_u = s(\sigma, \sigma_u)$, where

$$s(\sigma, \sigma_c) = \frac{1}{2} \left[1 - \tanh\left(\frac{\sigma - \sigma_c}{\delta} \right) \right]. \quad \text{(A2)}$$

The weather-layer potential temperature θ_w is given by Eq. (1), while the uppermost- and lowermost-layer potential temperatures θ_u and θ_l are given by

$$\theta_u = (\theta_p + \Delta_h - \Delta_z \log \sigma_u) r_u^{-\kappa}, \quad \text{(A3)}$$

$$\theta_l = \theta_p - \Delta_{zl} \log r_l, \quad \text{(A4)}$$

where $\kappa = 2/7$ is the adiabatic exponent, $r_u = \min(\sigma/\sigma_u, 1)$, and $r_l = \max(\sigma/\sigma_l, 1)$. The use of the maximum and minimum functions in the definitions of the effective sigma levels r_u and r_l means that θ_u and θ_l are constant in the weather layer and helps ensure that the weather layer remains statically stable. The parameters used were a polar temperature of $\theta_p = 260$ K, a transition depth $\delta = 0.07$, the layer separation levels $\sigma_u = 0.2$ and $\sigma_l = 0.6$, and a lowermost-layer static stability parameter $\Delta_{zl} = 50$ K.

The radiative damping coefficient k was specified as

$$k = k_{uw} s_l + k_l (1 - s_l), \quad \text{(A5)}$$

with $1/k_{uw} = 40$ days, and $1/k_l = 1$ day. Thus, the damping time has the same value in the weather layer and uppermost layer but is significantly shorter in the lowermost layer.

REFERENCES

Andrews, D. G., 1983: A finite-amplitude Eliassen–Palm theorem in isentropic coordinates. *J. Atmos. Sci.,* **40,** 1877–1883.

Busse, F. H., 1994: Convection driven zonal flows and vortices in the major planets. *Chaos,* **4,** 123–134.

Gutowski, W. J., 1985a: Baroclinic adjustment and midlatitude temperature profiles. *J. Atmos. Sci.,* **42,** 1733–1745.

——, 1985b: A simple model for the interaction between vertical eddy heat fluxes and static stability. *J. Atmos. Sci.,* **42,** 346–358.

Haynes, P. H., C. J. Marks, M. E. McIntyre, T. G. Shepherd, and K. P. Shine, 1991: On the "downward control" of extratropical diabatic circulations by eddy-induced mean zonal forces. *J. Atmos. Sci.,* **48,** 651–678.

Held, I. M., 1975: Momentum transport by quasigeostrophic eddies. *J. Atmos. Sci.,* **32,** 1494–1497.

——, 2000: The general circulation of the atmosphere. *Proc. Program in Geophysical Fluid Dynamics,* Woods Hole, MA, Woods Hole Oceanographic Institution. [Available online at http://hdl.handle.net/1912/15.]

——, and M. J. Suarez, 1994: A proposal for the intercomparison of the dynamical cores of atmospheric general circulation models. *Bull. Amer. Meteor. Soc.,* **75,** 1825–1830.

——, and V. D. Larichev, 1996: A scaling theory for horizontally homogeneous, baroclinically unstable flow on a beta plane. *J. Atmos. Sci.,* **53,** 946–952.

——, and T. Schneider, 1999: The surface branch of the zonally averaged mass transport circulation in the troposphere. *J. Atmos. Sci.,* **56,** 1688–1697.

Ingersoll, A. P., P. J. Gierasch, D. Banfield, A. R. Vasavada, and the Galileo Imaging Team, 2000: Moist convection as an energy source for the large-scale motions in Jupiter's atmosphere. *Nature,* **403,** 630–632.

——, and Coauthors, 2004: Dynamics of Jupiter's atmosphere. *Jupiter: The Planet, Satellites, and Magnetosphere,* F. Bagenal, T. E. Dowling, and W B. McKinnon, Eds., Cambridge University Press, 105–128.

Ioannou, P., and R. S. Lindzen, 1986: Baroclinic instability in the presence of barotropic jets. *J. Atmos. Sci.,* **43,** 2999–3014.

James, I. N., and L. J. Gray, 1986: Concerning the effect of surface drag on the circulation of a baroclinic planetary atmosphere. *Quart. J. Roy. Meteor. Soc.,* **112,** 1231–1250.

Lee, S., 2005: Baroclinic multiple zonal jets on the sphere. *J. Atmos. Sci.,* **62,** 2484–2498.

Lorenz, E. N., 1955: Available potential energy and the maintenance of the general circulation. *Tellus,* **7,** 157–167.

Panetta, R. L., 1993: Zonal jets in wide baroclinically unstable regions: Persistence and scale selection. *J. Atmos. Sci.,* **50,** 2073–2106.

Pedlosky, J., 1975: On secondary baroclinic instability and the meridional scale of motion in the ocean. *J. Phys. Oceanogr.,* **5,** 603–607.

——, 1979: Finite-amplitude baroclinic waves in a continuous model of the atmosphere. *J. Atmos. Sci.,* **36,** 1908–1924.

Porco, C., and Coauthors, 2003: Cassini imaging of Jupiter's atmosphere, satellites, and rings. *Science,* **299,** 1541–1547.

Rhines, P., 1975: Waves and turbulence on a beta-plane. *J. Fluid Mech.,* **69,** 417–443.

Schneider, T., 2005: Zonal momentum balance, potential vorticity dynamics, and mass fluxes on near-surface isentropes. *J. Atmos. Sci.,* **62,** 1884–1900.

——, 2007: The thermal stratification of the extratropical troposphere. *The Global Circulation of the Atmosphere,* T. Schneider and A. H. Sobel, Eds., Princeton University Press, 47–77.

——, and C. C. Walker, 2006: Self-organization of atmospheric macroturbulence into critical states of weak nonlinear eddy–eddy interactions. *J. Atmos. Sci.,* **63,** 1569–1586.

Simmons, A. J., and B. J. Hoskins, 1978: The life cycles of some nonlinear baroclinic waves. *J. Atmos. Sci.,* **35,** 414–432.

Smith, K., 2004: A local model for planetary atmospheres forced by small-scale convection. *J. Atmos. Sci.,* **61,** 1420–1433.

Stone, P. H., 1978: Baroclinic adjustment. *J. Atmos. Sci.,* **35,** 561–571.

——, and L. Branscome, 1992: Diabatically forced, nearly inviscid eddy regimes. *J. Atmos. Sci.,* **49,** 355–367.

Vallis, G., and M. Maltrud, 1993: Generation of mean flows and jets on a beta plane and over topography. *J. Phys. Oceanogr.,* **23,** 1346–1362.

Vasavada, A. R., and A. P. Showman, 2005: Jovian atmospheric dynamics: An update after Galileo and Cassini. *Rep. Prog. Phys.,* **68,** 1935–1996.

Williams, G. P., 2003a: Jet sets. *J. Meteor. Soc. Japan,* **81,** 439–476.

——, 2003b: Jovian dynamics. Part III: Multiple, migrating, and equatorial jets. *J. Atmos. Sci.,* **60,** 1270–1296.

Zhou, S., and P. H. Stone, 1993: The role of large-scale eddies in the climate equilibrium. Part II: Variable static stability. *J. Climate,* **6,** 1871–1881.